Chemical Engineering Journal 482 (2024) 148868

Contents lists available at ScienceDirect

Chemical Engineering Journal

journal homepage: www.elsevier.com/locate/cej

An asymmetric electrode matching reversible kinetics of oxygen reaction for a rechargeable Zn-air battery

Shuxin Li [a], Han Zhang [a,*], Lin Wu [a], Hongwei Zhao [a], Lin Tao [a], Lixiang Li [a,c,*], Chengguo Sun [a,b], Dongying Ju [c], Baigang An [a,c,*]

[a] Key Laboratory of Energy Materials and Electrochemistry Research Liaoning Province, School of Chemical Engineering, University of Science and Technology Liaoning, Anshan 114051, China
[b] School of Chemical Engineering, Nanjing University of Science and Technology, Nanjing 210094, China
[c] Hainan Provincial Key Lab of Fine Chemistry, School of Chemical Engineering and Technology, Hainan University, Haikou 570228, China

ARTICLE INFO

Keywords:
Asymmetric electrode
Multi-phase reaction
Aerophilic/hydrophilic interfacial
Reversible oxygen reaction
Zn-air battery

ABSTRACT

The development of zinc-air batteries (ZABs) is hindered by the sluggish kinetics of the oxygen reduction reaction (ORR) and the oxygen evolution reaction (OER) which occur in the complex interfaces between gaseous oxygen, liquid electrolyte and solid catalyst. Designing a rational interface that aligns with the kinetics of these multi-phase reactions is of utmost importance. Herein, an asymmetric cathode (Asy-electrode) has been designed and fabricated that the carbon nanotubes arrays (CNAs) encapsulating Co nanoparticles grown on carbon cloth is used as the aerophilic side (AI-side) to match and catalyze the ORR kinetics, the other side that deposition of NiFe layered double hydroxide (NiFe-LDH) on the CNAs plays as aerophobic side (AO-side) to accelerate the OER kinetics. The Asy-electrode effectively balances the adsorption and desorption of O_2 and OH^-, and promotes the efficient transport of gaseous and liquid reactants and products. Therefore, the efficiency of ORR and OER onto the corresponding catalytic sites of Co/CNAs and NiFe-LDH/CNAs are significantly enhanced. Consequently, the ZAB employing the asymmetric cathode can acquire a remarkable higher power density (236.26 mW cm^{-2}) and an excellent long-term cycling stability (over 1920 cycles at 10 mA cm^{-2}) due to the enhanced kinetic and the improved reversibility of the charge–discharge reaction on the cathode benefiting from the aerophilic/hydrophilic interfacial construction on each side of electrode. The present study could explore a route to design the catalysts from the view of matching the multi-phase reaction characteristics.

1. Introduction

Nowadays, the growing energy demands are boosting the development of high-efficiency energy storage systems combined with renewable sources [1–3]. Metal-air batteries, especially, are gaining significant attention as promising renewable energy technologies [4–6]. Particularly, rechargeable zinc-air battery (ZAB) is one of most desired energy system owing to its high energy density, minimal or zero emissions, simplicity in construction, and cost-effectiveness [7–10]. A conventional ZAB consists of an air cathode and a zinc metal anode. Here, the oxygen reduction reaction (ORR) and oxygen evolution reaction (OER) occur at the cathode during discharge and charge phases, respectively [11–15]. Because both kinetics of ORR and OER are sluggish, most efforts have been paid on developing high-efficiency bifunctional catalysts for ORR/OER [16–18]. The great progresses have been achieved from nanoclusters to single atomic sites, from heterostructure of multi-components to heteroatoms doping, from electronic orbits modulation to explore the intrinsic activity, and from improving utilization of active sites to enhancing the durability of catalysts [19–21]. However, the multi-phase gas-liquid-solid reactions in ORR and OER require the electrode have a rational design to supply the optimized interface matching the multi-phase reactions kinetics. Reports on achieving such electrodes are currently limited.

In the cathode of ZAB, the triple phase interface (TPI) of solid catalyst, liquid electrolyte, and gaseous reactant/product is critical for the catalytic reactions of ORR and OER [22,23]. A desirable architecture for the triple-phase catalytic systems should own the following characteristics (i) good accessibility to reagents; (ii) high intrinsic activity with

* Corresponding authors at: Key Laboratory of Energy Materials and Electrochemistry Research Liaoning Province, School of Chemical Engineering, University of Science and Technology Liaoning, Anshan 114051, China (L. Li and B. An).
E-mail addresses: hzhang0807@163.com (H. Zhang), lxli2005@126.com (L. Li), bgan@ustl.edu.cn (B. An).

https://doi.org/10.1016/j.cej.2024.148868
Received 13 October 2023; Received in revised form 20 December 2023; Accepted 16 January 2024
Available online 17 January 2024

abundant and stable active sites; (iii) an unobstructed mass-diffusion pathway and in-time release of as-formed intermediates and products. These have been partially demonstrated and verified for various heterogeneous catalysis including hydrogen evolution reaction [24], photocatalytic reaction [25], electrochemical generation of H_2O_2 [26], and reduction reaction of CO_2 [27].

It is well-established that when a catalyst is immersed into a liquid system, the interface between liquid and catalyst usually gives three typical wetting behaviors as illustrated in Fig. S1, Wenzel state (UW-state), Cassie state (UC-state) and Wenzel-Cassie coexistent state (UWC-state). The UW-state and UC-state, providing only two-phase interfaces, limit the efficiency of catalytic sites in contributing to gas-liquid-solid multiphase reactions. In contrast, under the UWC-state, the solid catalyst surface can be partially wetted by both liquid and the air trapped in the liquid to supply the triple-phase interface for multiphase reaction, which could bring more smooth kinetical processes for ORR and OER.

To achieve the UWC-state, a fundamental approach involves designing materials with asymmetrical aerophilic (hydrophobic) and aerophobic (hydrophilic) properties. For example, Janus materials owning the opposite property that have attracted considerable interests in various applications of switchable oil/water separation [28,29], fog harvesting [30], and sensors [31]. In ZABs, the ORR is a gas-consuming process. Therefore, ensuring an adequate supply of gas reactants at the interface is crucial. This facilitates the adsorption of reactants, interfacial charge transfer, and the desorption of intermediates/products at the active centers [32,33]. Correspondingly, aerophilic (hydrophobic) property is requisite for ORR. During OER process, gas bubbles are formed on the surface of electrodes. The aggregation of these bubbles around the catalysts can obscure active sites, significantly impeding the OER continuity. Therefore, it requires an aerophobic (hydrophilic) property for OER. Although it seems contradictory that ORR needs the aerophilic surface but OER requires aerophobic interface, as Janus materials generally possess opposite properties, an electrode could be designed to own both the aerophilicity and aerophobicity depending the composition and structure of each side. Additionally, optimizing or balancing the wettability of gas and liquid on the electrodes to align with the kinetics of ORR and OER could lead to highly energy-efficient, gas-liquid-solid heterogeneous catalysis processes.

Herein, an asymmetric electrode (referred to as Asy-electrode) balancing the aerophilic and hydrophilic properties of the interfaces has been successfully designed and fabricated. The carbon nanotubes arrays (CNAs) grown on both sides of the carbon cloth was using as the foundational electrode, in which Co nanoparticles were embedded inner of CNTs and play as the active sites for ORR. Moreover, the NiFe-LDH were controllably deposited on the other side of electrode to provide the hydrophilicity and the active sites for OER. This Asy-electrode design balances the contradictory requirements between the aerophilic and hydrophilic property to optimize the triple-phase interfaces for ORR and OER, and thus well match the reactions kinetics of cathode of ZAB. Consequently, the rechargeable ZAB with asymmetric cathode can deliver a remarkable power density of 236 mW cm^{-2}, a high capacity of 812 mAh g_{Zn}^{-1} and an excellent stability of 1920 cycles at 10 mA cm^{-2}.

2. Results and discussion

2.1. Materials structure and property

Fabrication of the Asy-electrode is schematically illustrated in Fig. 1. Firstly, the two-dimensional cobalt metal organic framework (2D Co-MOF) nanosheets with a strong bonding force on the smooth carbon cloth (CC) substrate were constructed (Fig. S2a) by a facile solution reaction of $Co(NO_3)_2$ and 2-methylimidazole. The scanning electron and transmission electron microscopy (SEM/TEM) images in Fig. 2a-b and Fig. S2b illustrate the vertically oriented Co-MOF nanosheet arrays grown on the CC surface. Then, the Co-MOF nanosheet arrays were heated up to a given temperature for 2 h under flowing Ar gas in a tube furnace containing dicyandiamide powders. The decomposition of dicyandiamide at 400 ℃ resulted in the formation of ammonia [34]. Under the reductive atmosphere of ammonia and the catalysis of Co, the Co-MOF nanosheets were in-situ transformed into the nitrogen-doped CNAs, while dicyandiamide as the nitrogen and carbon sources. As shown in Fig. 2c and Fig. S3a, the CC substrate surface is densely covered by the CNAs with the interconnected network structure replacing the previous Co-MOF nanosheets. The Co nanoparticles with a diameter about 13 nm are encapsulated inner of CNT, confirming that Co nanoparticles catalyzed the growth of CNTs (Fig. S3b-c), meanwhile Co particles act as the catalytic sites for ORR. Moreover, SEM images of Fig. 2d show that the CNAs rooted grow from the CC substrate. Since Co-MOFs arrays were vertically grown on both sides of CC by the wet chemical methods, the CNAs derived Co-MOFs are also produced on

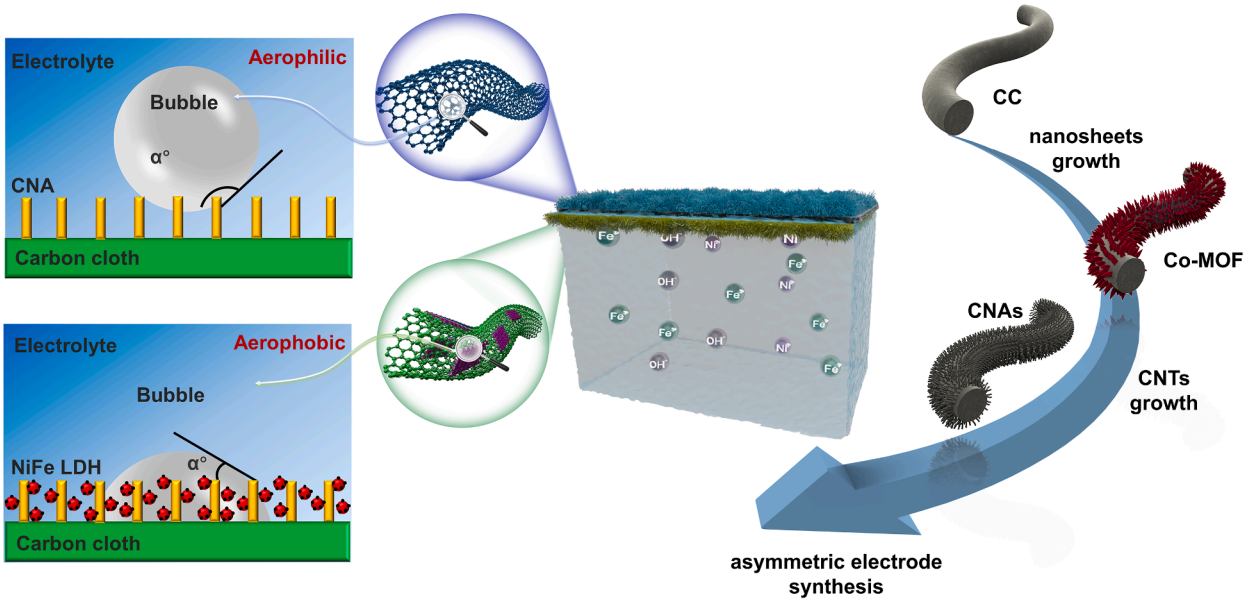

Fig. 1. Schematic illustration for the fabrication processes of asymmetric electrode and the modification mechanism by NiFe-LDH which starts from CNAs with aerophilic (AI) property to aerophobic (AO) parts.

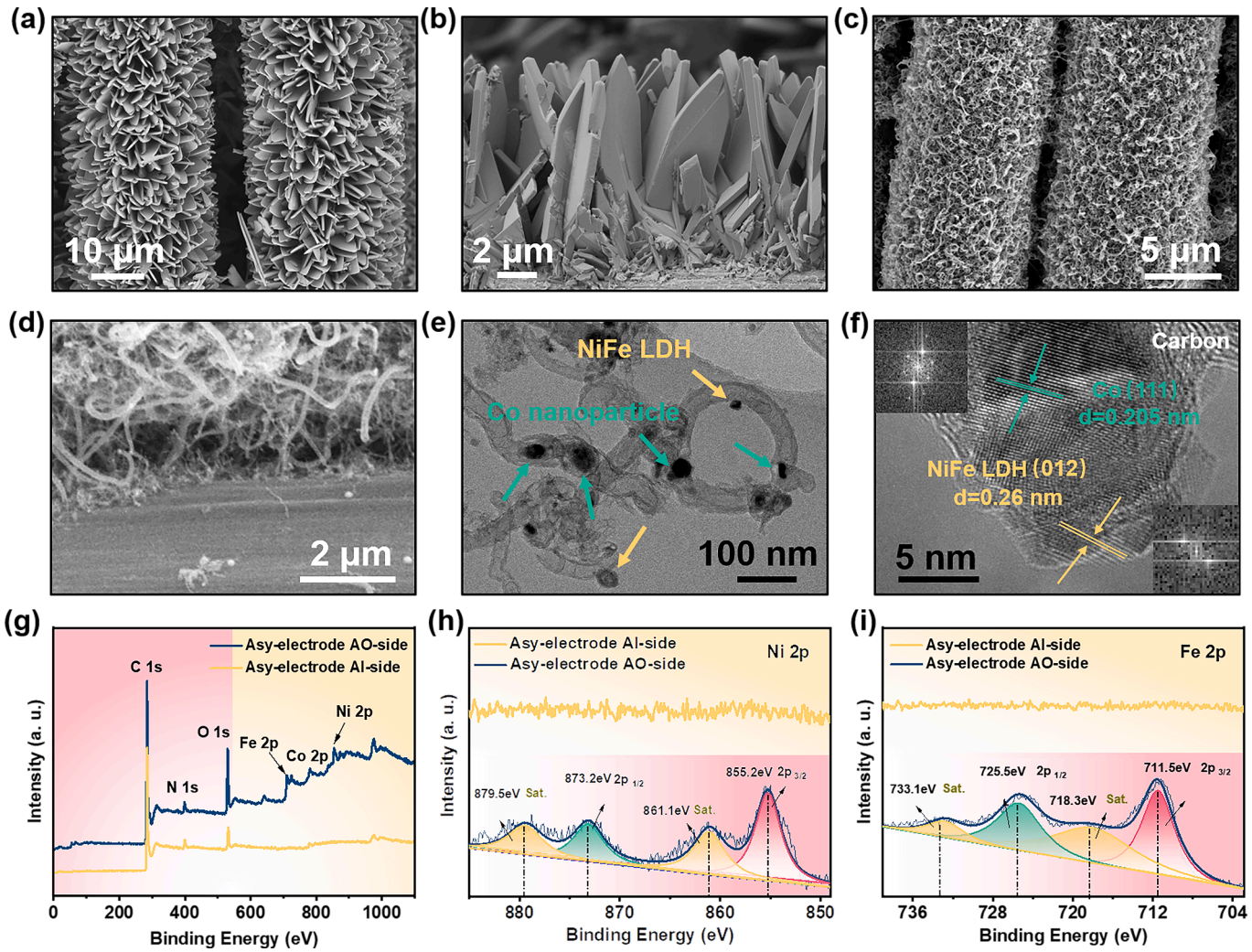

Fig. 2. (a and b) SEM images of Co-MOF, (c and d) SEM images of CNAs-Co@CC. (e) TEM and (f) HRTEM images of Asy-electrode AO-side. XPS spectra of the two sides of Asy-electrode: (g) Survey, (h) Ni 2p, and (i) Fe 2p regions.

both sides of CC. Consequently, the CNAs encapsulating Co nanoparticles inside the tubes grown on the CC (CNAs-Co@CC) supplies an expecting substrate to design an Asy-electrode.

Firstly, the highly graphitized CNAs offer unique hydrophobic property [35]. Subsequently, one side of CNAs-Co@CC plate was dipped in an alkaline aqueous solution containing Ni^{2+} and Fe^{3+} ions for 24 h at room temperature to form the NiFe layered double hydroxides (NiFe-LDH) onto the CNAs (Fig. S4), which can produce the hydrophilic/aerophobic side of CNAs-Co@CC electrode. The loading amounts of NiFe-LDH can be easily controlled by the dipping time to accurately regulate the hydrophilic property to balance the wettability of both side of electrode as shown in Fig. S5. The contact angle tests illustrate the enhanced hydrophility of the side containing the NiFe-LDH by prolonging the dipping time. It can also be noted that the side without the NiFe-LDH (0 h dipping) exhibits the largest contact angle of 123° due to the intrinsic hydrophobicity of CNAs. Therefore, it can conclude that the Asy-electrode with the amphoteric property has been constructed by the CNAs-Co@CC with and without the NiFe-LDH onto each side. The side of CNAs-Co@CC without NiFe-LDH is hydrophobic (aerophobic, referred as AI-side), but the side of CNAs-Co@CC with NiFe-LDH is hydrophilic (aerophobic, referred as AO-side). TEM was used to learn the amphoteric property of Asy-electrode from the microstructure. As shown in Fig. 2e, two types of particles can be observed in terms of Co nanoparticles being encapsulated in the CNAs, as well as the micro-sized NiFe-LDH particles being attached to the outer surface of CNAs. It can be further identified by the lattice fringes with interplanar spacings of 0.205 nm and 0.26 nm, corresponding to (1 1 1) and (0 1 2) crystal planes of the cubic cobalt and NiFe-LDH, respectively (Fig. 2f). Moreover, it can be clearly observed from the X-ray diffraction (XRD) pattern of Asy-electrode (Fig. S6). On the AO-side of Asy-electrode, the diffraction peaks at 2θ values of 11.7°, 23.7°, 34.7° are corresponding to the (0 0 3), (0 0 6), and (0 1 2) planes of the NiFe-LDH (JCPDS: 49–0188), respectively. Meanwhile, the typical diffraction peaks corresponding to (1 1 1) and (2 0 0) planes of metallic Co (JCPDS: 15–0806) at 44.2° and 51.5°. Hower, on the AI-side, only the diffraction peaks of Co can be observed. X-ray photoelectron spectroscopy (XPS) and energy-dispersive X-ray spectroscopy (EDX) elemental mappings were further used to investigate the difference in the composition between each side of the Asy-electrode. As displayed in Fig. 2g-i and Table S1, on the AO-side of Asy-electrode, Ni 2p and Fe 2p peaks can be easily observed. On the AI-side, however, neither Ni or Fe elements can be found. EDX analyses (Fig. S7) show the similar results that Ni and Fe are only distributed on the AO-side, uniformly. Moreover, C 1 s, N1s and Co 2p spectrum of both sides of Asy-electrode (Fig. S8a-c) show that there are no obvious components changes after NiFe-LDH modification.

To elucidate the aerophilic and hydrophilic property of each side of Asy-electrode from the molecular level, DFT [36,37] was used to calculate adsorption energy, adsorption distance, and electron density distribution of H_2O molecule on the CNT and NiFe-LDH. The configuration of NiFe-LDH [38–40] and CNT [41,42] was established as shown

in Fig. 3a and 3b, which assigns six sites to describe the adsorption behavior of H_2O molecules. As shown in Fig. 3c, all the adsorption sites of NiFe-LDH afford much higher adsorption energy than the adsorption sites of CNT. The adsorption energy of H_2O molecule on O-tp is significantly less than the other three adsorption points since Ni and Fe atoms have strong adsorption effects on H_2O molecule. However, two adsorption sites on CNT surface show the smaller adsorption energy for H_2O molecule. Fe atoms of NiFe-LDH possess the strongest adsorption energy and the shortest adsorption distance with H_2O molecule. Furthermore, the electron density distribution was calculated to determine the bonding situation at the liquid–solid interface. H_2O molecules show significant electron accumulation on NiFe-LDH surface due to their strong bond energy. In contrast, no electron accumulation occurs at the interface of H_2O molecules and CNT surface. The calculation results prove that NiFe-LDH has a strongly hydrophilic property, while CNT has a distinct hydrophobic property.

The wetting and aerophilic/aerophobic properties of the Asy-electrode are demonstrated as follow. The contact angle (CA) of a water droplet on the AI-side is 122° (Fig. 3d), whereas the CA is 37° for the AO-side (Fig. 3e). The asymmetric wettability of the Asy-electrode owes to the bi-directional structure of CNAs and NiFe-LDH on the contrary sides of electrode. The correlation between the hydrophobic/hydrophilic with the aerophilic/aerophobic can be directly expressed by the Young's equation [43]. The underwater bubble wettability was measured through the contact angle of bubble with the surfaces of Asy-electrode immersed in water. The bubble CAs on the AO-side and AI-side are 14° and 137°, respectively, showing the corresponding aerophilicity and aerophobicity of Asy-electrode. As another evidence, the color of the AI-side changes from initial darkness to mirror-like gray after immersion in basic solution (right picture in Fig. 3d), which arises from the air interlayer between the nanostructures of AI-side and the water interface that reflects most of light [44]. In contrast, the colour does not change a lot on the AO-side (right picture in Fig. 3e) due to its aerophobicity. The bubble contacting dynamic of the electrodes was further real-time observed as shown in Fig. S9. When oxygen bubbles touch the AI-side surface of Asy-electrode, the oxygen bubbles are suddenly burst, demonstrating the "aerophilic" property (Fig. S9a). In contrast, the AO-side is the bubbles repulsed, the bubbles keep the spherical shape and roll off from the surface of AO-side (Fig. S9b). The phenomena well demonstrate the aerophilic and the aerophobic behaviors brought by the asymmetric side of Asy-electrode. The side constructed by the vertically aligned carbon nanotubes arrays provides an "aerophilic" property and has a strong interaction toward oxygen bubbles, thereby could enhance ORR kinetics. The side containing NiFe-LDH shows a significant aerophobicity but good hydrophilicity, which could facilitate the OER kinetics. As shown in Fig. 3f-g, on the basis of the Laplace's theory, the hydrophobic-hydrophilic asymmetric structure on the two sides of Asy-electrode generates a difference capillary pressure (see the supplementary note in the Supporting Information for details).

2.2. Electrochemical characterization and discussion

To evaluate the effectiveness of the asymmetric wettability of electrode on improving the kinetics of ORR and OER, a series of electrochemical characterizations on Asy-electrode, AI-electrode (Fig. S10a), AO-electrode (Fig. S10b) and commercial Pt/C electrode were carried out (see Experimental section for details). As CV curves shown in Fig. S11 and Fig. S12, the oxygen reduction peak around 0.8 V can be evidently observed for the Asy-electrode under the O_2-saturated electrolyte, demonstrating the exceptional ORR electrocatalytic activity. The ORR performance of Asy-electrode was evaluated and compared with the other electrodes. As shown in Fig. 4a, the Asy-electrode exhibits

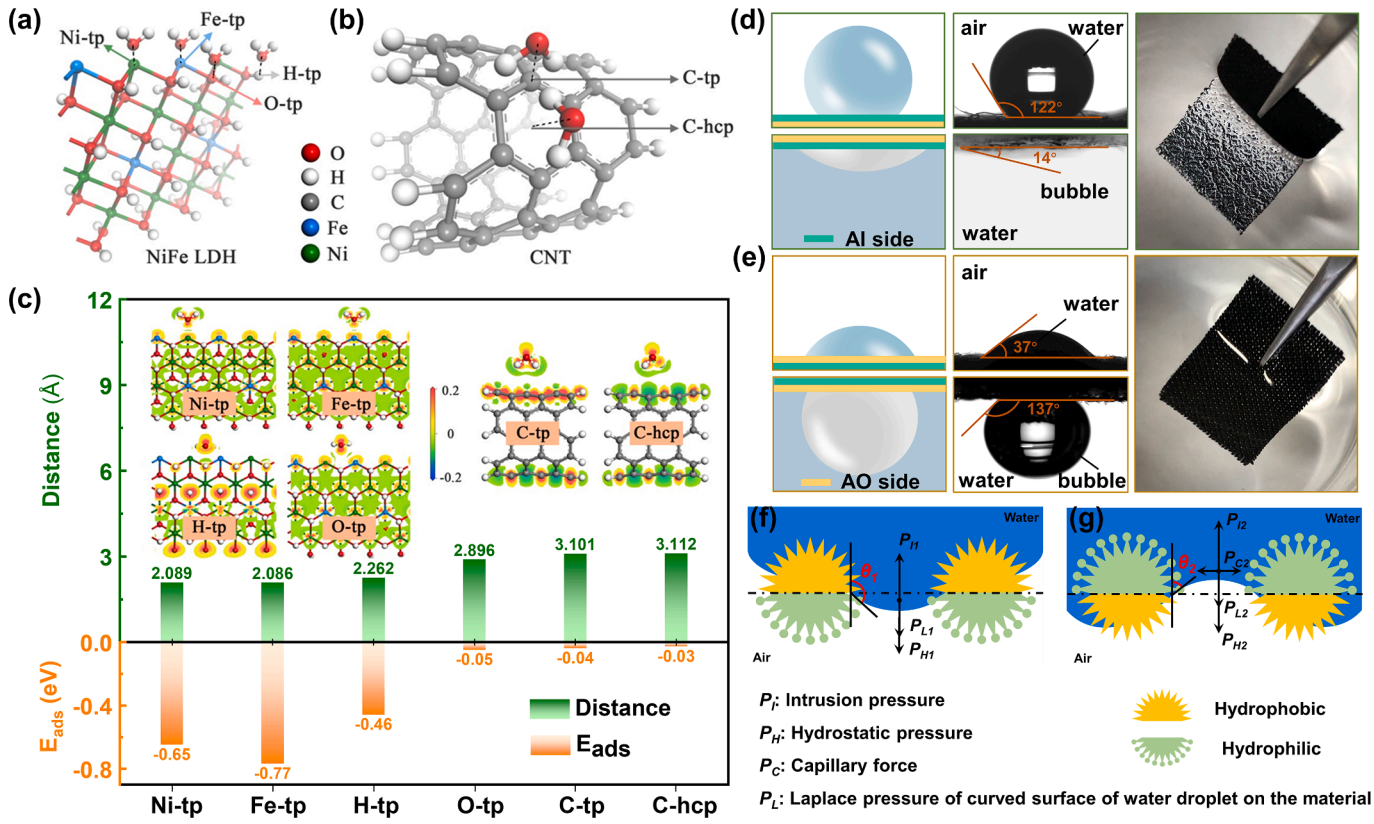

Fig. 3. Schematic diagram of the initial adsorption sites of on (a) NiFe-LDH and (b) CNT surface. (c) Adsorption distance and adsorption energy of H_2O molecules on different adsorption sites of the two types of materials (insert maps show the electron density distribution of interfacial interaction). (d and e) Digital camera images and optical pictures showing different wetting ability of the two sides of the Asy-electrode. (f and g) The force analysis of droplets on the hydrophobic layer and the hydrophilic layer.

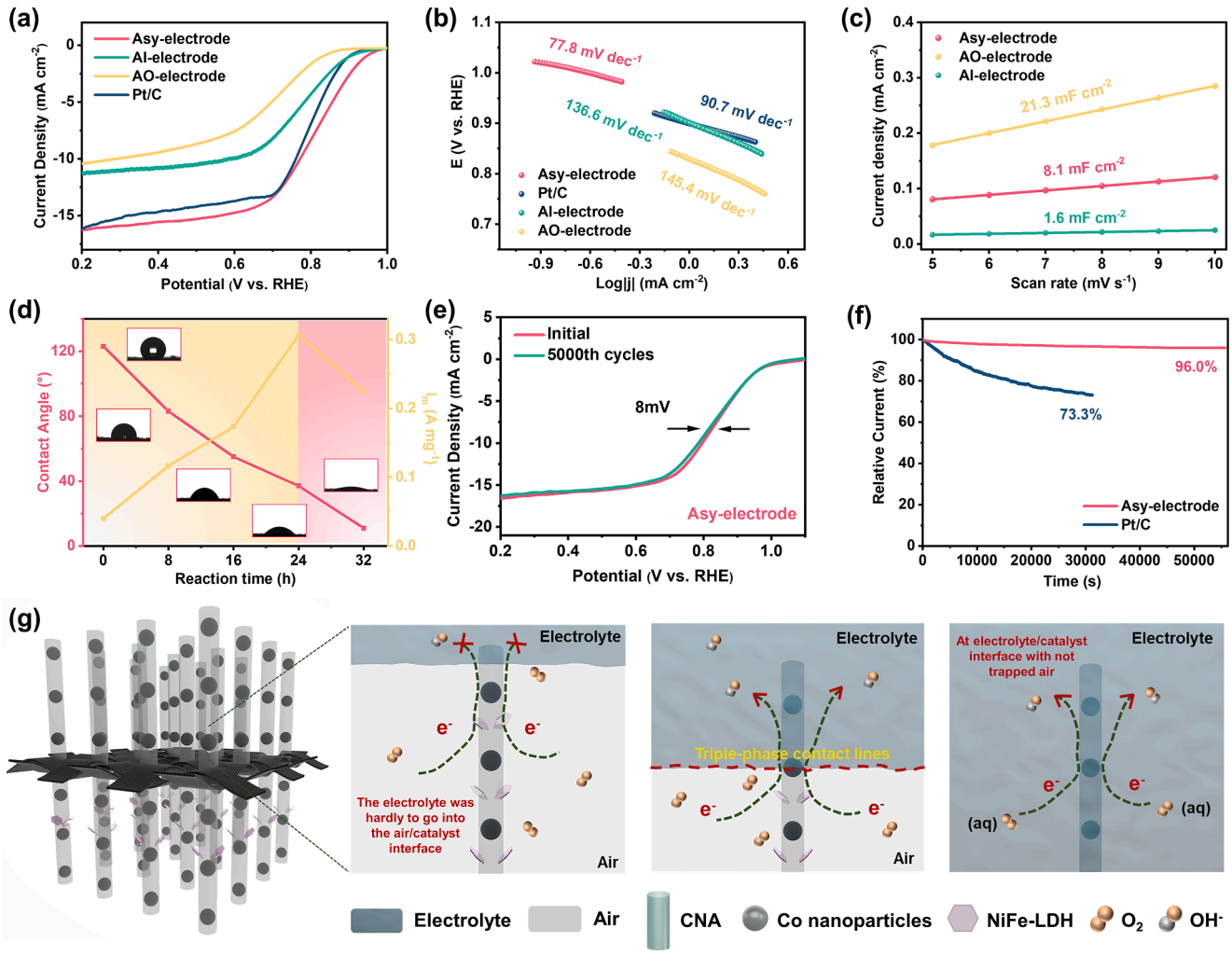

Fig. 4. (a) LSV curves, (b) Tafel plots derived from the ORR polarization curves and (c) C_{dl} values of Asy-electrode, AI-electrode, AO-electrode and Pt/C. (d) Plots of contact angles and mass activity for Asy-electrode with different reaction times. (e) LSV curves of Asy-electrode before and after 5000 cycles. (f) Stability tests on Asy-electrode and Pt/C electrode in O_2-saturated 0.1 M KOH carried out by chronoamperometry. (g) Schematic illustration of the three typical s wetting state of a catalyst surface can be labeled as the nature of gas/liquid/solid interface. The schematic diagram of TPI was denoted by the red dotted line.

an outstanding onset potential (E_{onset} = 0.97 V) and half-wave potential ($E_{1/2}$ = 0.81 V), which is much more positive than AI-electrode (E_{onset} = 0.93 V, $E_{1/2}$ = 0.77 V) and AO-electrode (E_{onset} = 0.88 V, $E_{1/2}$ = 0.72 V), even superior to the state-of-the-art Pt/C (E_{onset} = 0.94 V, $E_{1/2}$ = 0.79 V). Furthermore, Asy-electrode shows the larger limiting current density of 15.8 mA cm^{-2} at 0.3 V vs. RHE than AI-electrode (11.1 mA cm^{-2}), AO-electrode (9.9 mA cm^{-2}), and commercial Pt/C catalyst (15.2 mAcm^{-2}), illustrating that the amphoteric design on electrode is more favourable for gas diffusion and mass transfer. The kinetic behaviour of electrodes was evaluated by the Tafel slope. The Asy-electrode owns much lower Tafel slope of 77.8 mV dec^{-1} than AI-electrode (136.6 mV dec^{-1}), AO-electrode (145.4 mV dec^{-1}) and Pt/C catalyst (90.7 mV dec^{-1}), vindicating the faster reaction kinetics of Asy-electrode due to the matching wettability for the surface/interface reactions (Fig. 4b). Furthermore, the electron transfer mechanism of ORR on the electrodes was calculated according to Koutecky-Levich (K-L) equation. All the electrodes exhibit as a first-order reaction kinetics (Fig. S13). Comparing the electron transfer number (n) of AI-electrode (3.45) and AO-electrode (3.22), the ORR occurring at the Asy-electrode is the most efficiency reaction pathway with four electrons suggesting that the balance between the wettability of gas and liquid on the electrode is even critical for a fast reaction route.

Because only the liquid/solid interface can provide the adsorption/desorption sites of ions contributing to the electrical double layer capacitance (C_{dl}) [45], which was used as an indicator of the electrochemically active surface area (ECSA) to evaluate the wettable region of electrodes. As shown in Fig. S14, the C_{dl} values provide an evidence for the area of hydrophilic/hydrophobic interfaces. The C_{dl} value (1.6 mF cm^{-2}) of AI-electrode is much lower than AO-electrode (21.3 mF cm^{-2}, Fig. 4c), indicating that the aerophilic AI-electrode governs the interface to exclude most of hydrolytic ions. Contrastively, the aerophobic AO-electrode blocks gaseous reactants to attract most of electrolyte ions. Therefore, neither AO-electrode or AI-electrode facilitates the gas-liquid-solid triple-phase contact for ORR [46,47]. However, the Asy-electrode compromises the aerophility and aerophobility to get a C_{dl} of 8.1 mF cm^{-2} enlarging the gas-liquid-solid triple phase interface.

The correlation between the wetting property and ORR performance of electrodes were further investigated. As shown in Fig. 4d, the reaction time for NiFe-LDH modification on the surface of electrode increases from 0 h to 32 h, the water CA of the AO-side surface decreases from 123° to 11°, demonstrating the enhanced the hydrophilicity of electrode by the NiFe-LDH modification. The ORR mass activity of electrode is also improved by NiFe-LDH and reaches the maximum value of 0.31 A mg^{-1}at CA of 31°. Afterward, the mass activity decreases since the overmodified hydrophilicity causes the numerous liquid–solid interface to block the contact between the active sites and O_2. To check the possible influences of NiFe-LDH on the ORR performance, NiFe-LDH were directly grown onto CC substrate without the CNAs by different reaction time of 4, 8, 12

and 16 h (named as NiFe-LDH@CC, Fig. S15). Compared with the pristine CC, NiFe-LDH@CC appears a similar low ORR activity, the ORR performance reflected by LSV curves (Fig. S16) almost have no changes with the reaction time, confirming that the modification of NiFe-LDH primarily impacts the triple phase interface (TPI) by tuning hydrophilicity of electrode.

The TPI around electrode is of significant importance for implementing the intrinsic ability of catalysts. The AI-electrode with CNAs structure possesses the strong capacity of gas accommodation and the hydrophobicity, limiting the electrolyte infiltration. As schematic diagram of one piece of CNT shown in Fig. 4g. The aerophility arises numerous air-catalyst interface (UC-state) on the CNTs and the dense gas film makes electrolyte hardly to go into the reaction regions, resulting in an insufficient ion transport and the resultant poor ORR performance. Similarly, the AO-electrode leads to the poor gaseous feed in electrolyte-catalyst interface (showed as UW-state). Because of the solubility of oxygen gas in alkaline electrolyte is as low as 70 mg O_2/L, corresponding 4∼5 orders of magnitude lower than O_2 molecules dissolved in H_2O [48]. Asy-electrode balancing and optimizing the interfaces of gas-solid and liquid–solid gives rise to the decent TPI with the features of Wenzel Cassie coexistent state (UWC-state), which imposes a prominent impact on accelerating transmission between gas and liquid. Onto Asy-electrode, O_2 bubbles can be captured quickly by the aerophilic side to make ORR occur in the triple-phase region. While the hydrophilic side provides the access to electrolyte and release the resultant OH^- ions from ORR, smoothly. As a deduction, Asy-electrode whose AI-side serves as a gas reservoir, but AO-side plays as a good electrolyte/ion transporter, to enhance the ORR reaction kinetics. To demonstrate the advantages of asymmetric structure on the catalytic ORR, ORR stability was further measured. As shown in Fig. 4e and 4f, there is only a minor decay of $E_{1/2}$ for the electrode (8 mV decay in $E_{1/2}$) after 5000 cycles. The Asy-electrode presents an excellent long-term stability that 96.0 % of the initial current can be retained after 15 h operation at 0.6 V, which is significantly better than the commercial Pt/C (73.3 %). The chemical composition and structure of Asy-electrode after the ORR stability test were characterized and the results are shown in Fig. S17. It can be revealed by XPS that chemical composition of each side of the Asy-electrode is almost unchanged. Furthermore, according to the TEM observations, Co nanoparticles are still embedded in carbon nanotube and NiFe-LDH are still well attached around CNTs, suggesting that the Asy-electrode is stable during the ORR process.

The Asy-electrode also displays remarkable OER performance with a lower overpotential ($E_{j=10}$) of 280 mV at 10 mA cm^{-2} (Fig. 5a), which is superior to those of RuO_2 (410 mV), AI-electrode (360 mV), and AO-electrode (310 mV). Moreover, the Asy-electrode displays a Tafel slope of 124.8 mV dec^{-1}, which is remarkably lower than RuO_2 (150.7 mV dec^{-1}), AI-electrode (139.5 mV dec^{-1}), and AO-electrode (133.4 mV dec^{-1}), indicating the excellent kinetic and activity of OER (Fig. S18). EIS was also used to evaluate the charge transfer capabilities of the synthesized electrocatalysts. As shown in Fig. 5b and Table S2, the Nyquist plots show a distinct semicircle corresponding to the charge transfer resistance (R_{ct}), which reveals the lowest R_{ct} of Asy-electrode compared the other counterparts, indicating the enhanced kinetics of OER. Moreover, Asy-electrode exhibits an excellent stability that there is a little polarization increase after 3000 cycles and a 95.3 % of current retention after 28 h chronoamperometric operation (Fig. S19 and S20). To check the possible change of catalysts after the electrochemical oxidation environment, we compared the surface chemical states of the Asy-electrode by XPS before and after the OER stability test are shown in Fig. S21a-c. The Co 2p spectrum show no observable change after the OER process. The spectrum of Ni appears a significant characteristic peak of Ni^{3+} compared with the as-prepared Asy-electrode, which are ascribed to the NiOOH. As for Fe 2p spectrum show that the peaks of the binding energy at 711.5 eV and 725.5 eV correspond to the characteristics of Fe^{3+}, while the peaks are no obvious changes after OER test. In addition, the TEM images of the Asy-electrode after the OER test show

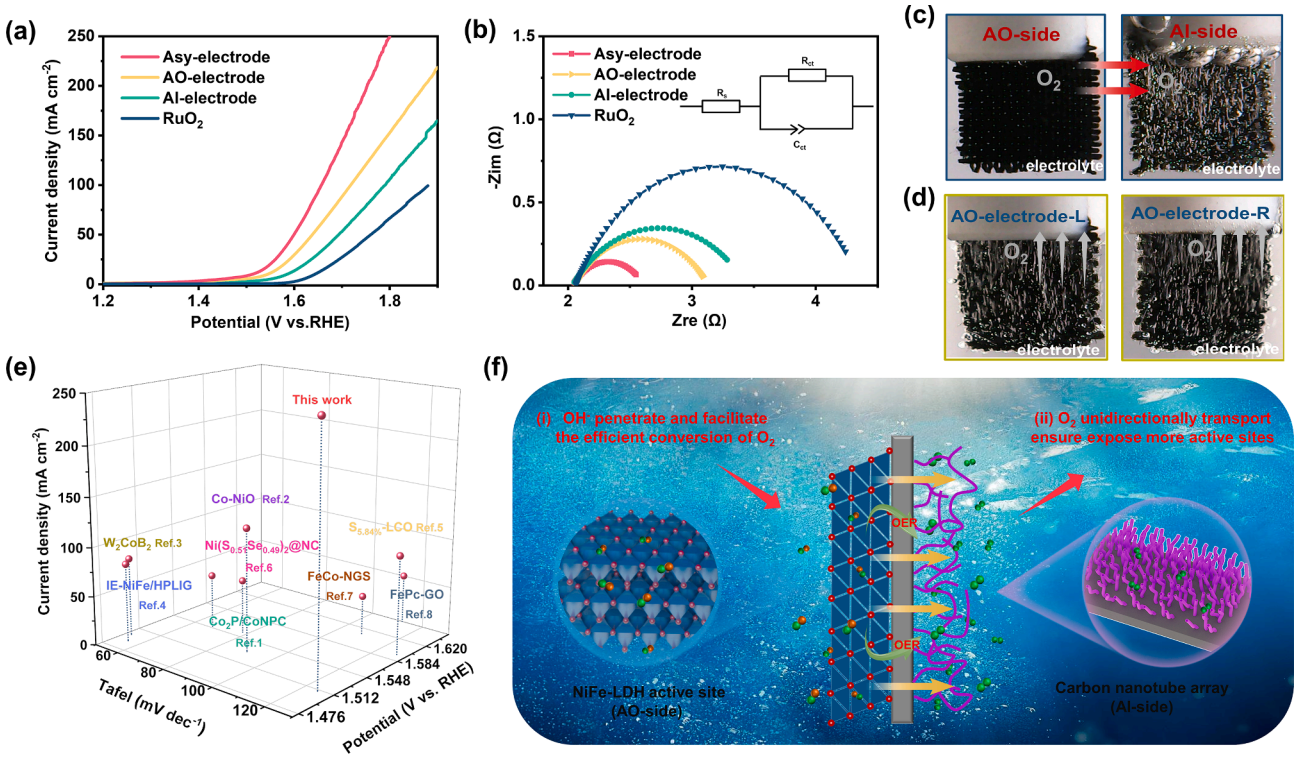

Fig. 5. (a) OER polarization curves, and (b) electrochemical impedance spectroscopy (EIS) of Asy-electrode, AI-electrode, AO-electrode and RuO_2, the inset is the fitting circuits of electrodes. Digital camera images of the two sides of (c) the Asy-electrode and (d) the AO-electrode submerged in the electrolyte. (e) OER performance comparisons in terms of the Tafel values (*x*-axis), the potential at 10 mA cm^{-2} (*y*-axis), and the current density (*z*-axis) between Asy-electrode and other reported electrodes recently. (f) The schematic illumination of TPI unidirectional gas evolution.

that the carbon nanotubes morphology can be well retained, indicating the structure robustness of the Asy-electrode (Fig. S21d). The HR-TEM image (Fig. S21e-f) further provides more persuasive evidence that clear lattice spacing of 0.341 nm corresponding to the (1 2 0) plane of NiFeOOH, are observed attached to the outer surface of carbon nanotubes. Meanwhile, it can be seen that Co is still indexed by lattice spacing of 0.20 nm of the (1 1 1) plane.

To assess the gas diffusion property towards OER, Asy-electrode was submerged in the electrolyte by using a three-electrode system (Fig. 5c). During the charging tests, an plenty of oxygen bubbles were observed on the AI-side, but no apparent bubbles generated on the AO-side. It can be clearly observed that the bubbles were always transported from the AO-side to the AI-side of Asy-electrode, indicating that the resultant O_2 bubbles by OER on hydrophilic AO-side spontaneously transport to the aeropholic AI-side. Due to the suitable wettability, the newly formed O_2 bubbles can adhere to the triple phase interface (TPI) through lateral resistance. This adherence, primarily stabilized by the TPI on the aerophobic (AO) side, results in increased bubble pressure. Additionally, bubble deformation occurs as a consequence of asymmetric wettability, leading to a variance in Laplace pressure. This differential creates the driving force necessary for unidirectional gas transport (Fig. S22 and S23). Such a unidirectional gas evolution process allows the generated O_2 gas to depart from the active sites quickly, to boost the kinetics of OER. In contrast (Fig. 5d), the both sides of AO-electrode displayed an abundance of gas bubbles that engulfed the entire surface of electrode. The dense O_2 gas film onto the electrode makes OH^- ions hardly to contact with the active sites, resulting in a limited OER performance.

To illustrate the advantages of Asy-electrode design, some previously reported air electrodes for OER performance were compared. As shown in Fig. 5e, the optimized electrode structure exhibits the highest OER activity with the lowest overpotential at 10 mA cm^{-2}, the smallest value of Tafel slope and the largest current density. To reveal the effect of asymmetric interface of the electrode on OER, the schematic illustration is shown in Fig. 5f. When Asy-electrode was submerged in the basic electrolyte, the AO-side can adsorb abundant OH^- due to the hydrophilicity, and then the adsorbed OH^- on the active sites are catalytically oxidized into gaseous O_2. Subsequently, the generated O_2 can be unidirectional transported to AI-side, and thus the active sites can be fully exposed to the following OER.

2.3. Rechargeable Zn-Air battery performance

Asy-electrode has displayed highly efficient and stable electrochemical activity on ORR or OER. As a bifunctional electrode on both ORR and OER, the voltage gap ($\Delta E = E_{j=10} - E_{1/2}$) between the OER potential at 10 mA cm^{-2} and the half-wave potential for the ORR are the

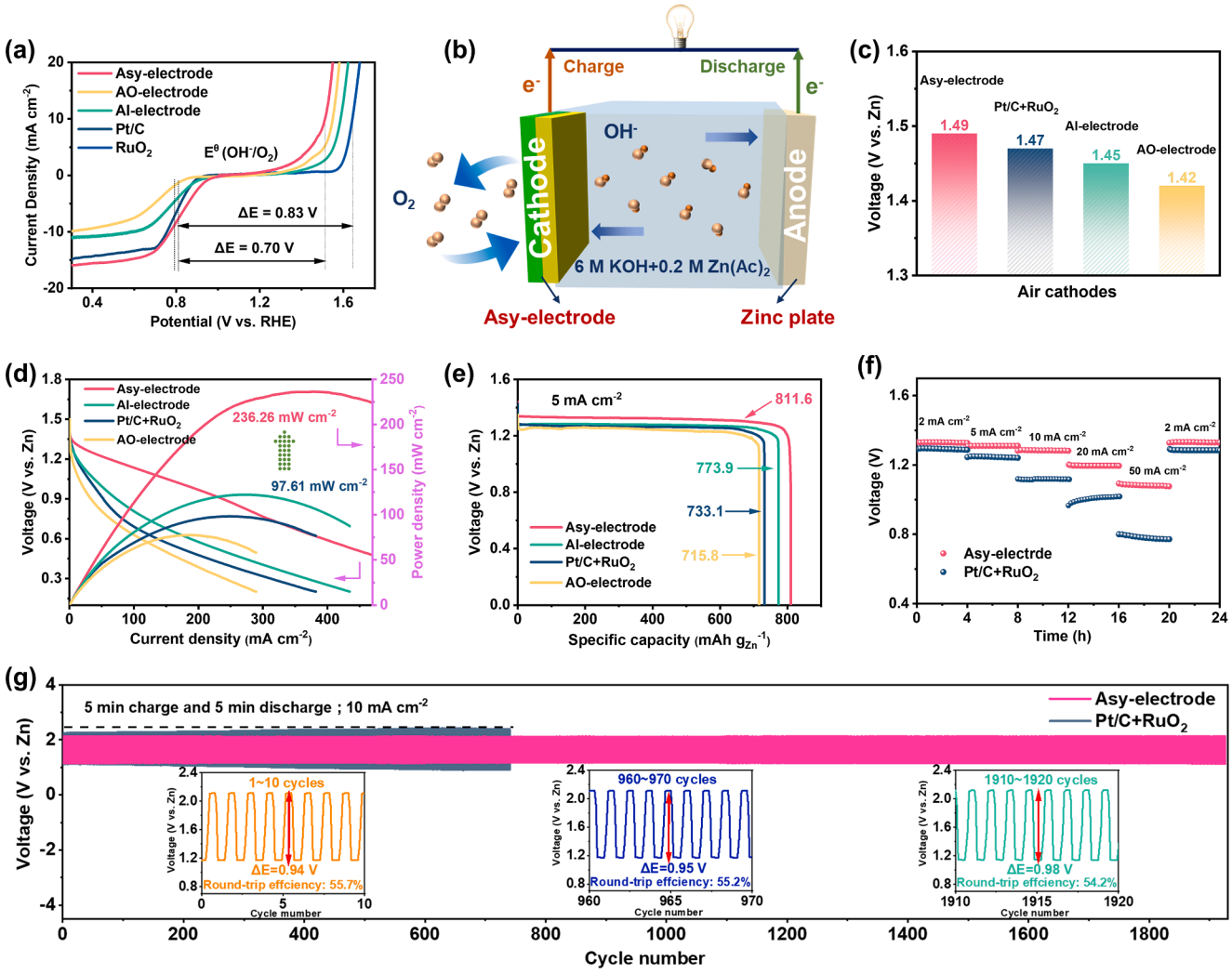

Fig. 6. (a) The overall LSV curves for ORR and OER of Asy-electrode, AO-electrode, AI-electrode and Pt/C + RuO_2 electrode. (b) Schematic illustration of the zinc-air battery using Asy-electrode. (c) The open-circuit voltage, (d) discharging polarization curves and corresponding power density plots, and (e) the specific capacity of the Asy-electrode, AO-electrode, AI-electrode and Pt/C + RuO_2 electrode as the air cathode, respectively. (f) Galvanostatic discharge curves, and (g) discharge–charge cycling curves of ZABs at 10 mA cm^{-2} with Asy-electrode.

crucial parameters for the overall bifunctional catalytic activity. A lower value of ΔE suggests the better bifunctional catalytic performance and is desirable for practical applications in rechargeable metal-air batteries. Remarkably, the ΔE value was determined to be only 0.70 V for Asy-electrode, which is significantly lower than Pt/C + RuO_2 electrode (Fig. 6a). The bifunctional electrocatalytic activity with respect of ΔE is presented in Table S3, Asy-electrode behaves superior to those of most reported non-precious metal-based catalysts, suggesting aerophilic and hydrophilic side design of cathode matching ORR and OER kinetics well to improve the reversibility of charge–discharge.

Overall performance of a rechargeable Zn-air battery assembling the Asy-electrode was assessed (Fig. 6b and Fig. S24). As illustrated in Fig. 6c, the ZAB delivers an open-circuit voltage up to 1.49 V, which is higher than ZABs with Pt/C + RuO_2 electrode (1.47 V), AI-electrode (1.45 V) or AO-electrode (1.42 V). The discharge–charge curves of the ZABs (Fig. S25) further reveal that using the Asy-electrode has the smaller voltage gap, and the higher current density at all potential compared to the ZABs with Pt/C + RuO_2 electrode, AI-electrode or AO-electrode. Fig. 6d shows the discharge curves and the corresponding power density curves of ZABs. ZAB with the Asy-electrode delivers a preeminent peak power density of 236.26 mW cm^{-2}, which significantly exceeds the ZAB with the Pt/C + RuO_2 electrode about three times. As shown in Fig. 6e, the specific capacity of the ZAB driven by the Asy-electrode reaches 811.6 mA h g_{Zn}^{-1} at 5 mA cm^{-2}, it is much higher than the ZABs with Pt/C + RuO_2 electrode (733.1 mA h g_{Zn}^{-1}), AI-electrode (773.9 mA h g_{Zn}^{-1}) or AO-electrode (715.8 mA h g_{Zn}^{-1}). Rate performance of battery is highly related with the transfer of electrons and ions. As shown in Fig. 6f, ZAB with Asy-electrode has high output voltages of 1.33 V-1.19 V at the current density from 2 to 50 mA cm^{-2}. Cycling stability was further investigated by the galvanostatic discharge–charge curves of ZABs (Fig. 6g and S26). Comparing with the poor cyclable ZAB with the Pt/C + RuO_2 electrode, the ZAB with the Asy-electrode exhibits the low voltage gap (0.94 V) of the initial discharge–charge, a high round-trip efficiency (55.7 %) at 10 mA cm^{-2} and an excellent stability (stable operation of 320 h). In overall performance, ZAB matching the Asy-electrode surpassed those recently reported rechargeable ZABs using novel catalysts (Table S4).

According to the characteristics of charge–discharge reactions of ZABs, during the charge process, the hydrophilic NiFe-LDH catalysts can enhance the OH^- ions adsorption and thus accelerate OER kinetics. The generated O_2 from OER are simultaneously transported to the aerophilic side of cathode, avoiding the blocks of active sites by O_2 bubbles. During the discharge process, the carbon nanotube arrays structures with aerophilic property can further boost the adsorption and conversion of O_2 at the catalytic active site to enhance the catalytic efficiency. The hydrophilic product of OH^- can be rapidly desorbed due to the hydrophobic property of AI-side. Therefore, O_2 can be continuously transported to the catalyst surface to enhance ORR reaction kinetics. This novel asymmetric structure design of cathode improves the reversibility of the charge–discharge reaction by matching the reactions kinetic in ZABs and thus could be applied in developing those battery systems relating to the multi-phase reactions.

3. Conclusion

An asymmetric electrode (Asy-electrode) has been successfully designed to balance the wettability of gas and liquid on solid catalysts for the optimizing the gas-liquid-solid multi-phase interfaces for ORR and OER. The Asy-electrode was basically constructed by the carbon nanotube arrays (CNAs) grown on carbon cloth in which Co nanoparticles was embedded in the inner of CNT, therefore the electrode supplies the aerophilic property by CNTs and ORR catalytic activity by Co nanoparticles. Additionally, the unilateral modification with NiFe-LDH imparts hydrophilic properties and OER activity to the electrode. Precise control over this single-sided NiFe-LDH modification allows for an optimal balance between aerophilicity and hydrophilicity, creating an enhanced Wenzel-Cassie coexistent state (UWC-state) that expands the triple-phase reaction interface. Consequently, the Asy-electrode effectively aligns with the cathode kinetics of ZABs, promoting the diffusion of reactants and products (oxygen and OH^-), and facilitating efficient adsorption and conversion during both ORR (discharge) and OER (charge) processes. Therefore, the rechargeable ZABs using the asymmetric cathodes greatly increases the concentration of reactants at the interface, accelerates mass transfer, and strengthens the interfacial stability. An impressive high power density of 236.26 mW cm^{-2}, coupled with an extended cycling life of 1920 cycles at 10 mA cm^{-2}, has been successfully achieved. The present study provides a strategy to the triple-phase catalytic reactions systems for various energy storage systems by matching the interfacial reaction kinetics.

CRediT authorship contribution statement

Shuxin Li: Data curation, Formal analysis, Writing – original draft. **Han Zhang:** Formal analysis, Methodology, Resources, Conceptualization. **Lin Wu:** Conceptualization, Formal analysis. **Hongwei Zhao:** Supervision. **Lin Tao:** Conceptualization, Formal analysis. **Lixiang Li:** Funding acquisition, Project administration, Supervision. **Chengguo Sun:** Supervision, Visualization. **Dongying Ju:** Project administration, Validation. **Baigang An:** Funding acquisition, Investigation, Project administration, Writing – review & editing.

Declaration of competing interest

The authors declare that they have no known competing financial interests or personal relationships that could have appeared to influence the work reported in this paper.

Data availability

Data will be made available on request.

Acknowledgements

The financial supports from National Natural Science Foundation of China (NSFC, No. 52872131, 51972156, 52304330 and 22109061), The specific research fund of the Innovation Platform for Academicians of Hainan Province (YSPTZX202315), National Natural Science Foundation of Liaoning Province (2022-BS-283), Technology Liaoning Talent Project Grants (601010326), Key Project supported by the Research Foundation of Education Bureau of Liaoning Province (No. JYTZD2023093), Distinguished Professor Project of Education Department of Liaoning and the Open Project Found of Key Laboratory of Energy Materials and Electrochemistry Liaoning Province are acknowledged.

Appendix A. Supplementary data

Supplementary data to this article can be found online at https://doi.org/10.1016/j.cej.2024.148868.

References

[1] H. Liu, J. Guan, S. Yang, Y. Yu, R. Shao, Z. Zhang, M. Dou, F. Wang, Q. Xu, Metal-organic-framework-derived Co2P nanoparticle/multi-doped porous carbon as a trifunctional electrocatalyst, Adv. Mater. 32 (36) (2020) 2003649.
[2] X. Sun, S. Wang, Y. Hou, X.F. Lu, J. Zhang, X. Wang, Self-supporting metal-organic framework-based hydrogen and oxygen electrocatalysts, J. Mater. Chem. A 11 (25) (2023) 13089–13106.
[3] X. Han, N. Li, J.S. Baik, P. Xiong, Y. Kang, Q. Dou, Q. Liu, J.Y. Lee, C.S. Kim, H. S. Park, Sulfur mismatch substitution in layered double hydroxides as efficient oxygen electrocatalysts for flexible zinc-air batteries, Adv. Funct. Mater. 33 (11) (2023) 2212233.
[4] W. Tang, K. Teng, W. Guo, F. Gu, B. Li, R. Qi, R. Liu, Y. Lin, M. Wu, Y. Chen, Defect-engineered Co3O4@nitrogen-deficient graphitic carbon nitride as an efficient

bifunctional electrocatalyst for high-performance metal-air batteries, Small 18 (2022) 2202194.
[5] S. Hu, M. Zhu, Semiconductor for oxygen electrocatalysis in photo-assisted rechargeable zinc-air batteries: Principles, advances, and opportunities, Energy Storage Mater. 61 (2023) 102866.
[6] Z. Nie, L. Zhang, Q. Zhu, Z. Ke, Y. Zhou, T. Wågberg, G. Hu, Reversed charge transfer induced by nickel in Fe-Ni/Mo_2C@nitrogen-doped carbon nanobox for promoted reversible oxygen electrocatalysis, J. Energy Chem. 88 (2024) 202–212.
[7] Y. Zhang, D. Wu, F. Huang, Y. Cai, Y. Li, H. Ke, P. Lv, Q. Wei, "Water-in-salt" nonalkaline gel polymer electrolytes enable flexible zinc-air batteries with ultra-long operating time, Adv. Funct. Mater. 32 (2022) 2203204.
[8] J. Han, H. Bao, J.-Q. Wang, L. Zheng, S. Sun, Z.L. Wang, C. Sun, 3d N-doped ordered mesoporous carbon supported single-atom Fe-N-C catalysts with superior performance for oxygen reduction reaction and zinc-air battery, Appl. Catal. B Environ. 280 (2021) 119411.
[9] Y. Li, Y. Ding, B. Zhang, Y. Huang, H. Qi, P. Das, L. Zhang, X. Wang, Z.-S. Wu, X. Bao, N, O symmetric double coordination of an unsaturated fe single-atom confined within a graphene framework for extraordinarily boosting oxygen reduction in Zn-air batteries, Energy Environ. Sci. 16 (6) (2023) 2629–2636.
[10] F. Yang, J. Xie, X. Liu, G. Wang, X. Lu, Linker defects triggering boosted oxygen reduction activity of Co/Zn-ZIF nanosheet arrays for rechargeable Zn-air batteries, Small 17 (3) (2021) 2007085.
[11] X. Han, T. Zhang, W. Chen, B. Dong, G. Meng, L. Zheng, C. Yang, X. Sun, Z. Zhuang, D. Wang, Mn-N_4 oxygen reduction electrocatalyst: Operando investigation of active sites and high performance in zinc–air battery, Adv. Energy Mater. 11 (6) (2021) 2002753.
[12] P. Anand, M.-S. Wong, Y.-P. Fu, Perovskite oxide composites for bifunctional oxygen electrocatalytic activity and zinc-air battery application- a mini-review, Energy Storage Mater. 58 (2023) 362–380.
[13] J. Liu, Z. Luo, X. Zhang, H. Zheng, L. Peng, D. Qian, C. Jia, D. Sun-Waterhouse, G. I. Waterhouse, FeCoNi nanoalloys embedded in hierarchical N-rich carbon matrix with enhanced oxygen electrocatalysis for rechargeable Zn-air batteries, J. Mater. Chem. A 9 (48) (2021) 27701–27708.
[14] Z. Li, L. Zhang, Q. Zhu, Z. Ke, G. Hu, Spatial separation strategy to construct N/S co-doped carbon nanobox embedded with asymmetrically coupled Fe-Co pair-site for boosted reversible oxygen electrocatalysis, J. Colloid Interface Sci. 653 (2024) 1577–1587.
[15] R. He, L. Yang, Y. Zhang, X. Wang, S. Lee, T. Zhang, L. Li, Z. Liang, J. Chen, J. Li, A. Ostovari Moghaddam, J. Llorca, M. Ibáñez, J. Arbiol, Y. Xu, A. Cabot, A CrMnFeCoNi high entropy alloy boosting oxygen evolution/reduction reactions and zinc-air battery performance, Energy Storage Mater. 58 (2023) 287–298.
[16] H.W. Go, T.T. Nguyen, Q.P. Ngo, R. Chu, N.H. Kim, J.H. Lee, Tailored heterojunction active sites for oxygen electrocatalyst promotion in zinc-air batteries, Small 19 (10) (2023) 2206341.
[17] X. Zhong, Y. Shao, B. Chen, C. Li, J. Sheng, X. Xiao, B. Xu, J. Li, H.-M. Cheng, G. Zhou, Rechargeable zinc-air batteries with an ultralarge discharge capacity per cycle and an ultralong cycle life, Adv. Mater. 35 (30) (2023) 2301952.
[18] J. Hong, M. Chen, L. Zhang, L. Qin, J. Hu, X. Huang, C. Zhou, Y. Zhou, T. Wågberg, G. Hu, Asymmetrically coupled Co Single-atom and Co nanoparticle in Double-shelled Carbon-based nanoreactor for enhanced reversible oxygen catalysis, Chem. Eng. J. 455 (2023) 140401.
[19] J.C. Li, Y. Meng, L. Zhang, G. Li, Z. Shi, P.X. Hou, C. Liu, H.M. Cheng, M. Shao, Dual-phasic carbon with Co single atoms and nanoparticles as a bifunctional oxygen electrocatalyst for rechargeable Zn–air batteries, Adv. Funct. Mater. 31 (42) (2021) 2103360.
[20] S. Li, H. Zhang, L. Wu, H. Zhao, L. Li, C. Sun, B. An, Vacancy-engineered CeO_2/Co heterostructure anchored on the nitrogen-doped porous carbon nanosheet arrays vertically grown on carbon cloth as an integrated cathode for the oxygen reduction reaction of rechargeable Zn-air battery, J. Mater. Chem. A 10 (18) (2022) 9858–9868.
[21] L. Wu, S. Li, L. Li, H. Zhang, L. Tao, X. Geng, H. Yang, W. Zhou, C. Sun, D. Ju, B. An, Modest modulation on the electronic structure of Co_9S_8 by vanadium doping for high-performance rechargeable Zn-air batteries, Appl. Catal. B Environ. 324 (2023) 122250.
[22] L. Yan, B. Xie, C. Yang, Y. Wang, J. Ning, Y. Zhong, Y. Hu, Engineering self-supported hydrophobic–aerophilic air cathode with CoS/Fe_3S_4 nanoparticles embedded in S, N Co-doped carbon plate arrays for long-life rechargeable Zn-air batteries, Adv. Energy Mater. 13 (10) (2023) 2204245.
[23] T. Zhou, H. Shan, H. Yu, C.A. Zhong, J. Ge, N. Zhang, W. Chu, W. Yan, Q. Xu, H. A. Wu, C. Wu, Y. Xie, Nanopore confinement of electrocatalysts optimizing triple transport for an ultrahigh-power-density zinc-air fuel cell with robust stability, Adv. Mater. 32 (47) (2020) 2003251.
[24] Y. Wang, Y. Zou, L. Tao, Y. Wang, G. Huang, S. Du, S. Wang, Rational design of three-phase interfaces for electrocatalysis, Nano Res. 12 (9) (2019) 2055–2066.
[25] X. Sheng, Z. Liu, R. Zeng, L. Chen, X. Feng, L. Jiang, Enhanced photocatalytic reaction at air-liquid-solid joint interfaces, J. Am. Chem. Soc. 139 (36) (2017) 12402–12405.
[26] S. Wang, D. Ye, H. Liu, X. Zhu, Q. Lan, Y. Yang, R. Chen, Q. Liao, Engineering a concordant microenvironment with air-liquid-solid interface to promote electrochemical H_2O_2 generation and wastewater purification, Sep. Purif. Technol. 297 (2022) 121527.
[27] Q. Zhang, Y. Xia, S. Cao, "Environmental phosphorylation" boosting photocatalytic CO_2 reduction over polymeric carbon nitride grown on carbon paper at air-liquid-solid joint interfaces, Chinese J. Catal. 42 (10) (2021) 1667–1676.
[28] M. Alvisi, M. Blome, M. Griepentrog, V.-D. Hodoroaba, P. Karduck, M. Mostert, M. Nacucchi, M. Procop, M. Rohde, F. Scholze, The determination of the efficiency of energy dispersive X-ray spectrometers by a new reference material, Microsc. Microanal. 12 (5) (2006) 406–415.
[29] Y.S. Lee, B.K. Kaang, N. Han, H.-J. Lee, W.S. Choi, An anti-overturn Janus sponge with excellent floating stability for simultaneous pollutant remediation and oil/water separation, J. Mater. Chem. A 6 (34) (2018) 16371–16381.
[30] W. Zhou, C. Zhou, H. Yang, J. Wang, J. Du, L. Chen, H. Shen, L. Tan, L. Dong, X. Zeng, Janus copper mesh with asymmetric wettability for on-demand oil/water separation and direction-independent fog collection, J. Environ. Chem. Eng. 9 (5) (2021) 105899.
[31] H. Han, S. Baik, B. Xu, J. Seo, S. Lee, S. Shin, J. Lee, J.H. Koo, Y. Mei, C. Pang, T. Lee, Bioinspired geometry-switchable Janus nanofibers for eye-readable H_2 sensors, Adv. Funct. Mater. 27 (29) (2017) 1701618.
[32] M. Wang, S. Medina, J.R. Pfeilsticker, S. Pylypenko, M. Ulsh, S.A. Mauger, Impact of microporous layer roughness on gas-diffusion-electrode-based polymer electrolyte membrane fuel cell performance, ACS Appl. Energy Mater. 2 (11) (2019) 7757–7761.
[33] Z.-L. Wang, D. Xu, J.-J. Xu, X.-B. Zhang, Oxygen electrocatalysts in metal-air batteries: from aqueous to nonaqueous electrolytes, Chem. Soc. Rev. 43 (22) (2014) 7746–7786.
[34] L. Liu, Y. Wang, F. Yan, C. Zhu, B. Geng, Y. Chen, S.L. Chou, Cobalt-encapsulated nitrogen-doped carbon nanotube arrays for flexible zinc-air batteries, Small Methods 4 (1) (2020) 1900571.
[35] F. Fei, X. Zhou, S. Wang, M. Li, X. Cao, N. Yuan, J. Ding, Tunning of optimal parameters for growth of spinnable carbon nanotube arrays at a relatively low temperature and pressure, Carbon 192 (2022) 452–461.
[36] S. Nie, J. Li, L. Tao, Y. He, D. Dastan, X. Meng, P. Poldorn, X. Yin, Insights into selective mechanism of NiO-TiO_2 heterojunction to H_2 and CO, ACS Sensors 8 (11) (2023) 4121–4131.
[37] L. Tao, D. Dastan, W. Wang, P. Poldorn, X. Meng, M. Wu, H. Zhao, H. Zhang, L. Li, B. An, Metal-decorated InN monolayer senses N_2 against CO_2, ACS Appl. Mater. Interfaces 15 (9) (2023) 12534–12544.
[38] B. Zhang, C. Zhu, Z. Wu, E. Stavitski, Y.H. Lui, T.-H. Kim, H. Liu, L. Huang, X. Luan, L. Zhou, Integrating rh species with NiFe-layered double hydroxide for overall water splitting, Nano Lett. 20 (1) (2019) 136–144.
[39] H. Xiao, H. Shin, W.A. Goddard III, Synergy between Fe and Ni in the optimal performance of (Ni, Fe)OOH catalysts for the oxygen evolution reaction, Proc. Natl. Acad. Sci. USA 115 (23) (2018) 5872–5877.
[40] B.M. Hunter, W. Hieringer, J. Winkler, H. Gray, A. Müller, Effect of interlayer anions on [NiFe]-LDH nanosheet water oxidation activity, Energy Environ. Sci. 9 (5) (2016) 1734–1743.
[41] X. Chen, L. Luo, Y. Zhang, Identification of the active sites of $NiCo_2O_4$ and the support effect with carbon nanotubes for oxygen reduction catalysis, Langmuir 37 (20) (2021) 6330–6336.
[42] E.Y. Li, N. Marzari, Improving the electrical conductivity of carbon nanotube networks: A first-principles study, ACS Nano 5 (12) (2011) 9726–9736.
[43] J. Yu, W. Chen, K. Li, C. Zhang, M. Li, F. He, L. Jiang, Y. Li, W. Song, C. Cao, Graphdiyne nanospheres as a wettability and electron modifier for enhanced hydrogenation catalysis, Angew. Chem. Int. Ed. 61 (34) (2022) e202207255.
[44] Z. Lu, W. Xu, J. Ma, Y. Li, X. Sun, L. Jiang, Superaerophilic carbon-nanotube-array electrode for high-performance oxygen reduction reaction, Adv. Mater. 28 (33) (2016) 7155–7161.
[45] S. Liu, Z. Cao, Y. Meng, Y. Li, W. Yang, Z. Chang, W. Liu, X. Sun, Aerophilic Co-embedded N-doped carbon nanotube arrays as highly efficient cathodes for aluminum-air batteries, ACS Appl. Mater. Interf. 13 (23) (2021) 26853–26860.
[46] Y.-J. Wang, D.P. Wilkinson, J. Zhang, Noncarbon support materials for polymer electrolyte membrane fuel cell electrocatalysts, Chem. Rev. 111 (12) (2011) 7625–7651.
[47] S. Park, J.-W. Lee, B.N. Popov, A review of gas diffusion layer in PEM fuel cells: Materials and designs, Int. J. Hydrogen Energy 37 (7) (2012) 5850–5865.
[48] J. Li, Y. Zhu, W. Chen, Z. Lu, J. Xu, A. Pei, Y. Peng, X. Zheng, Z. Zhang, S. Chu, Breathing-mimicking electrocatalysis for oxygen evolution and reduction, Joule 3 (2) (2019) 557–569.